Journal of
Marine Science
and Engineering

Essay

A Study on the Law of Ring-Shear Band Evolution

Jiyan Qiao, Xiaobing Lu * and Xuhui Zhang

Institute of Mechanics, Chinese Academy of Sciences, Beijing 100190, China
* Correspondence: xblu@imech.ac.cn

Abstract: A separate-bottom Couette cell is used to carry out ring-shear tests on sand and hydrate, and the evolution of shear bands is recognized using the tracer method. Based on experimental verification, a numerical simulation method is applied to study the shear band variation law with the height and strength of the sample. Analyzing the distribution of stress and strain gives a dimensionless number $(c + \rho g H \cdot tg\varphi)H/\alpha GL$ that affects the characteristics of the shear band, which indicates that the evolution direction and form of the shear band are controlled by the stiffness ratio of strength to load. Furthermore, the dimensionless law of the height and width of the shear band is given quantitatively.

Keywords: Couette cell; shear band; stiffness ratio

check for updates

Citation: Qiao, J.; Lu, X.; Zhang, X. A Study on the Law of Ring-Shear Band Evolution. *J. Mar. Sci. Eng.* **2023**, *11*, 70. https://doi.org/10.3390/jmse11010070

Academic Editors: Dejan Brkić and José-Santos López-Gutiérrez

Received: 13 November 2022
Revised: 10 December 2022
Accepted: 16 December 2022
Published: 2 January 2023

1. Introduction

Researches on the shear band of geomaterials include generally theoretical research, experimental research, and numerical simulation. M. Lätzel et al. [1] present experiments along with molecular-dynamics (MD) simulations of a two-dimensional (2D) granular material in a Couette cell undergoing slow shearing, and show the extent to which quantitative agreement between an experiment and MD simulation is possible. Lu Xiaobing et al. [2] theoretically analyzed the shear-band width of saturated soil under simple shear and coupled loads and obtained the approximate calculation formula for shear-band width. Borja R I et al. [3] carried out theoretical research on sand shear zones with the spatial distribution of density and obtained the law of the influence of material inertia on shear flow.

In terms of experiments, Sebastian Lobo-Guerrero et al. [4] developed laboratory ring-shear tests using sugar as a weak granular material. It was found that the residual friction coefficient of the material maintained a constant value regardless of the severe degradation of the particles, and the grain size distribution of the original uniform material evolved toward a fractal distribution of sizes. Wang Fenjia et al. [5] obtained shear characteristic curves for sliding zone soil of different water content under the action of ring shear at different shear rates. By experimental tests conducted with a ring-shear test apparatus, Motoyuki Suzuki et al. [6] elucidated the residual strength characteristics of artificial bedding planes that model the actual behavior of slip surfaces occurring between two layers with different degrees of cementation. Lv Xilin et al. [7] carried out a series of ring-shear tests under consolidation and drainage conditions and obtained the relation curve between the shear angle and shear stress of soil samples. Zhang Yiying et al. [8] carried out a ring-shear test with different water content and the shear rate of sliding zone soil in order to study the influence of water content and landslide sliding rate on the mechanical strength of sliding zone soil.

In terms of numerical simulations, Cundall and Strack [9] used discrete element software to simulate the shear zone of soil and obtained consistent results with the disk photoelastic test. Jiang Mingjing et al. [10] introduced the micro-cementation model of deep-sea energy soil into the discrete element software PFC2D, simulated the plane strain biaxial test of typical deep-sea energy soil, and compared it with uncemented samples under the same conditions to study the formation process of shear bands and the corresponding macro–micro mechanism of deep-sea energy soil. Huang Wenbo [11] used PFC2D discrete element software to carry out the numerical simulation of the biaxial compression test for a sand particle medium and PFC3D discrete element software to carry out the numerical simulation of sand particle single-shear flow under periodic boundary conditions. Wencheng Jin et al. [12] proposed a modified Drucker-Prager/Cap (MDPC) model enhanced with density dependence, and full-size 3D Schulze ring-shear tests were modeled in Abaqus with calibrated model parameters. The simulated Mohr-Coulomb envelopes matched well with the experimental results, indicating that the stress state within the shear band of the ring-shear test was close to triaxial compression.

2. Test Design

2.1. Set of Test

The separate-bottom Couette cell [13] used is composed of a shear cylinder, servo drive device, and numerical control unit, among which the shear cylinder is the core part. The shear cylinder is composed of an inner and an outer cylinder. The inner cylinder can rotate under the drive, and the outer cylinder is fixed on the base. The inner and outer cylinders are connected in close contact with each other, and the O-type rubber ring is placed between them to play a waterproof role.

In order to ensure that there is no relative sliding on the contact surface between the sample and the shear cylinder, rectangular tooth grooves are engraved on the bottom surface of the inner cylinder and the side wall of the rotating shaft to increase the static friction. Figure 1 shows the real figure of the Couette cell.

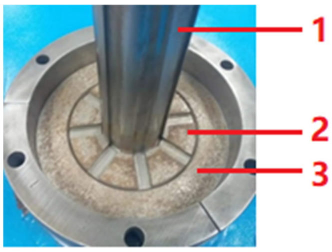

Figure 1. Couette cell used in the experiments. 1—rotating shaft; 2—inner cylinder; 3—outer cylinder.

2.2. Test Process

Three types of dry sand of different particle sizes and hydrate were used as the test samples, and the stacking height of the samples was changed during the test. In order to observe the sample movement trajectory on the surface, black tracers were arranged on the sample surface along the radial direction, which takes advantage of the axisymmetric shape of the shear cylinder. This is shown in Figure 2.

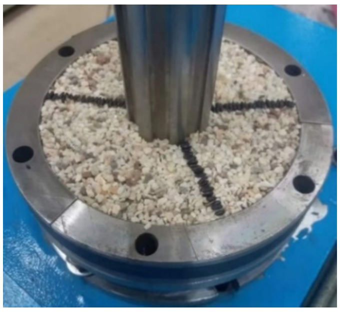

Figure 2. Placement of black tracer.

First, the physical and mechanical parameters of the samples were determined by triaxial tests and acoustic tests, as shown in Table 1.

Table 1. Parameters of test samples.

Medium	Particle Size (mm)	Cohesion (kPa)	Friction Angle (Degree)	Elasticity Modulus (MPa)
Coarse sand	3.0	0	32	3.7
Medium sand	1.0	0	39	4.0
Fine sand	0.25	0	44	4.6
Hydrate	——	510	28	70.0

2.2.1. Tests of Different Strengths for Sand

Three types of dry sand of different particle sizes were used under the condition of stacking height H = 3 cm.

i. Test of coarse sand

When the inner cylinder is rotated at different angles, changes in tracer lines are shown in Figure 3, where A represents the angle (in degrees).

(**a**) A = 44 (**b**) A = 132

(**c**) A = 544 (**d**) A = 800

Figure 3. Tests of coarse sand: (**a**) rotation angle is 44°; (**b**) rotation angle is 132°; (**c**) rotation angle is 544°; (**d**) rotation angle is 800°.

According to Figure 3a–d, there is no relative sliding between the sample and the outer cylinder. At a point along the radial line between the inner and outer cylinder, the tracer particles are deformed due to ring shear (Figure 3a). As the deformation increases, the particles in the deformation area have both annular and radial motions, so the motion trajectory becomes a spiral shape (Figure 3b). When the deformation continued to increase, the regular helical trajectory line disappeared, and the tracer particles assumed an irregular distribution (Figure 3c,d). In a ring strip near the edge of the outer cylinder, the tracer particles are not disturbed and the tracing lines remain straight. However, in the inner cylinder, the tracer particles are arranged orderly along the rotation direction.

ii. Test of medium sand

The changes in tracer lines are shown in Figure 4, where A represents the angle (in degrees).

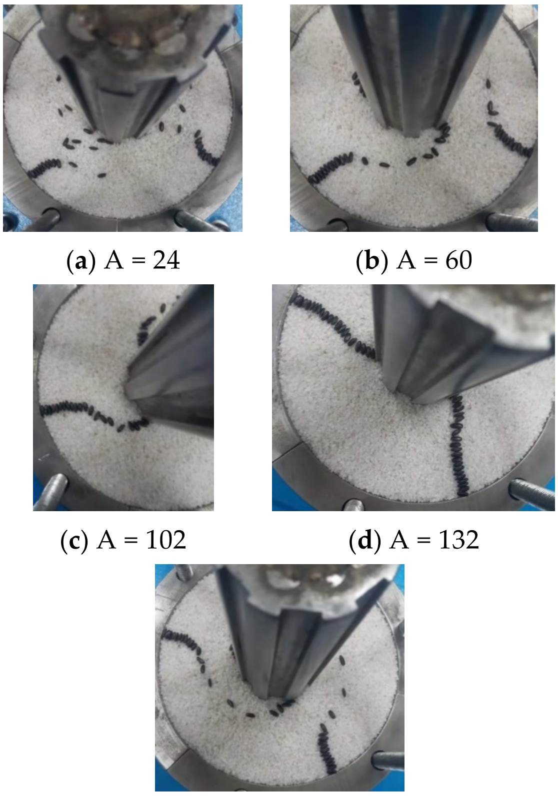

(**a**) A = 24 (**b**) A = 60

(**c**) A = 102 (**d**) A = 132

(**e**) A = 540

Figure 4. Tests of medium sand: (**a**) rotation angle is 24°; (**b**) rotation angle is 60°; (**c**) rotation angle is 102°; (**d**) rotation angle is 132°; (**e**) rotation angle is 540°.

According to Figure 4a–e, the main change process of tracer-line shape is similar to that of coarse sand, which also experienced discontinuity, a spiral shape, and an irregular distribution. However, the difference is that the tracer lines are rotated at smaller angles when they appear the same shape. When the steady state is reached, the rotation angle is smaller, and also the disturbed area is smaller but the undisturbed area is larger.

iii. Test of fine sand

The changes in tracer lines are shown in Figure 5, where A represents the angle (in degrees).

According to Figure 5a–d, compared with coarse and medium sand, the tracer lines of fine sand experience smaller rotation angles when similar morphological changes occur. When the steady state is reached, the rotation angles are smaller and the sample is disturbed in a smaller area.

Now analyze the comparisons between test i, ii, and iii. The density of dry sand with three different particle sizes is similar and the stacking height is the same. The stress caused by gravity is approximately ~0.6 kPa, which is relatively close. However, because $\varphi_{fine} > \varphi_{middle} > \varphi_{coarse}$, coarse sand has the lowest macro strength and the most obvious deformation under shear disturbance. In terms of the evolution direction of the shear band, the comparison between tests i, ii, and iii shows that under the same stacking height of the sample, the higher the strength, the more the shear band will develop toward the inner ring wall, while the larger, undisturbed area will be toward the outer ring wall.

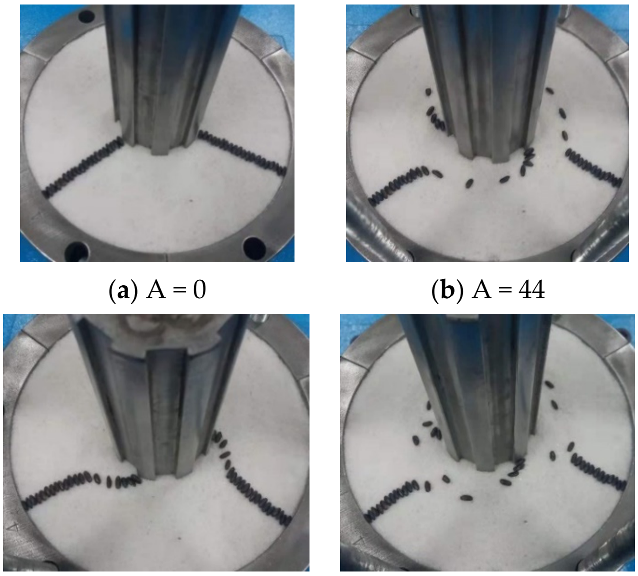
(**a**) A = 0 (**b**) A = 44 (**c**) A = 96 (**d**) A = 220

Figure 5. Tests of fine sand: (**a**) rotation angle is 0°; (**b**) rotation angle is 44°; (**c**) rotation angle is 96°; (**d**) rotation angle is 220°.

2.2.2. Tests of Different Stacking Heights for Sand

The shear tests of coarse sand and fine sand were carried out at different stacking heights of H = 1 cm, H = 3 cm, and H = 6 cm, respectively.

i. Test of coarse sand

The test process is the same as that in Section 2.2.1. The morphology of samples with different stacking heights when they reach stability is shown in Figure 6.


(**a**) H = 1.0 cm (**b**) H = 3.0 cm


(**c**) H = 6.0 cm

Figure 6. Tests of coarse sand: (**a**) stacking height is 1.0 cm; (**b**) stacking height is 3.0 cm; (**c**) stacking height is 6.0 cm.

According to Figure 6a–c, when H = 1 cm, the shear deformation region appears in a band of a certain width near the junction of the inner and outer cylinders. When H = 3 cm and H = 6 cm, the shear deformation region develops gradually to the wall of the rotating shaft. Correspondingly, the undisturbed area near the outer ring wall increases with the increase in the stacking height, which obviously indicates that the shear deformation is conducive to the evolution of the inner ring with the increase in the stacking height.

ii. Test of fine sand

The stable morphology of samples with different stacking heights is shown in Figure 7.

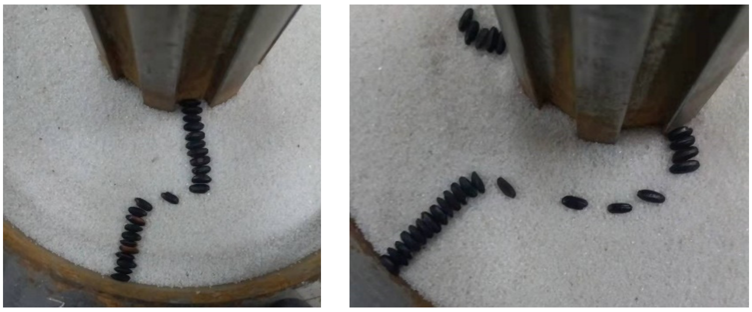

(**a**) H = 1.0 cm (**b**) H = 3.0 cm

(**c**) H = 6.0 cm

Figure 7. Tests of fine sand: (**a**) stacking height is 1.0 cm; (**b**) stacking height is 3.0 cm (**c**) stacking height is 6.0 cm.

According to Figure 7a–c, when H = 1 cm, the sample surface is disturbed by shear only in a very narrow area near the junction of the inner and outer shear cylinders, while no shear deformation occurs in other areas. With the increase in sample stacking height, when H = 3 cm, the width of the sample subjected to shear disturbance increases, and the area of shear disturbance develops to the inner side. When H = 6 cm, a large width in the direction of the outer ring is undisturbed, while the shear deformation region develops to the side wall of the inner ring.

According to the comparison between test i and test ii, it can be found that under the condition of the same sample, when the stacking height of the sample is small, the shear band can develop vertically to the surface and form a band of a certain width. With the increase in stacking height, the shear disturbance develops in the medial direction, while the undisturbed area pointing to the lateral direction is larger.

2.2.3. Tests of Different Stacking Heights for Hydrate

In this section, the ring-shear tests are carried out for hydrate at different stacking heights. Figure 8 shows the shear phenomenon of hydrate, in which the stacking heights are H = 4 cm, H = 2 cm, H = 1 cm, and H = 0.5 cm respectively.

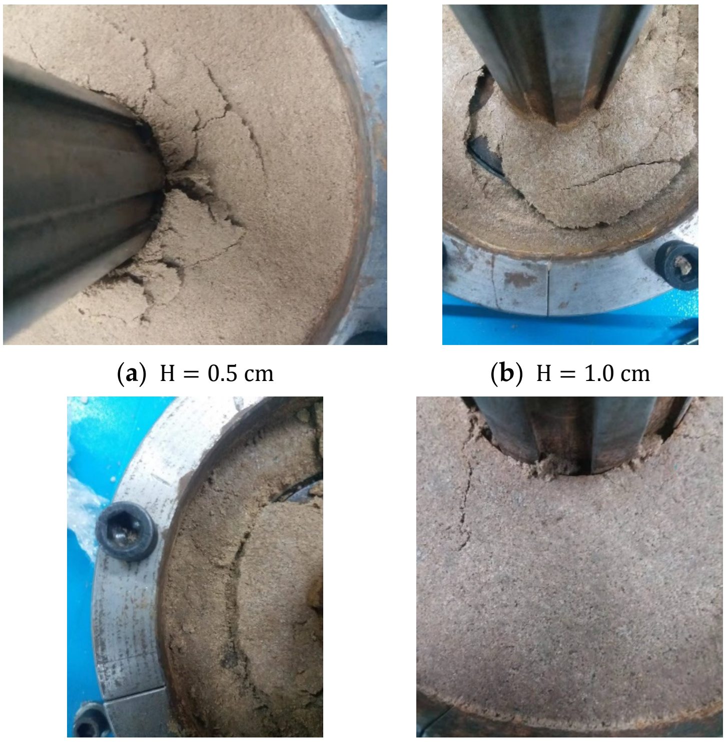
(**a**) H = 0.5 cm (**b**) H = 1.0 cm
(**c**) H = 2.0 cm (**d**) H = 4.0 cm

Figure 8. Tests of hydrate: (**a**) stacking height is 0.5 cm; (**b**) stacking height is 1.0 cm; (**c**) stacking height is 2.0 cm; (**d**) stacking height is 4.0 cm.

When the sample stacking height is very small, a shear band appears near the boundary between the inner and outer cylinder (Figure 8a). With the increase in stacking height, the shear band expands towards the inner cylinder (Figure 8b,c). However, when the sample stacking height is large, the shear band can only occur at the inner edge of the inner cylinder (i.e., the wall of the rotating shaft, Figure 8d). This is very similar to what happens for the sand ring-shear tests. The only difference is that the shear band of the hydrate is manifested as a brittle fracture and shows non-uniformity because uniformity is difficult to control very well when laying the hydrate sample.

3. Numerical Simulation and Analysis

Based on experimental phenomena, this section studies the law of shear band evolution with the variation in sample parameters including stacking height, cohesion, and internal friction angle by means of numerical simulation. In the calculation, the inner cylinder rotation angle was kept as a constant value, and the finite element software FEPG [14] was applied.

3.1. Constitutive Model

Under small deformations, the triaxial stress–strain relationship follows Hooke's law; namely:

$$\varepsilon_1 = \frac{1}{E}[\sigma_1 - \mu(\sigma_2 + \sigma_3)] \tag{1}$$

where σ_1 is axial stress, σ_2 and σ_3 are confining stresses, ε_1 is axial strain, and E and μ are the elastic modulus and Poisson's ratio, respectively.

In the conventional triaxial stress state:

$$\sigma_2 = \sigma_3 \tag{2}$$

$$\Delta\sigma = E\varepsilon_1 - (1 - 2\mu)\sigma_3 \tag{3}$$

where $\Delta\sigma = \sigma_1 - \sigma_3$, is deviatoric stress.

Wu Erlin et al. [15] established elastic model considering damage, in which the nominal stress in the constitutive relationship of non-damaged materials is replaced by the equivalent stress after damage, so the constitutive relationship can be obtained as follows:

$$\Delta\sigma = E(1-D)\varepsilon_1 - (1-2\mu)\sigma_3 \tag{4}$$

where D is the damage variable.

Assuming that the damage of material follows the Weibull distribution [16], then D can be deduced as follows:

$$D = 1 - exp\left[-\left(\frac{\varepsilon_1}{a}\right)^n\right] \tag{5}$$

where n is named as the shape parameter, $a = \varepsilon_f(1/n)^{-1/n}$, and ε_f is the peak strain.

3.2. Numerical Simulation

3.2.1. Verification

The experiment results in Section 2.2.2 (Figure 7) are taken as references to verify the numerical simulation. Numerical results show that the distribution form, width, and center position of the simulated shear bands are in good agreement with the experiment. In Figure 9, the red area represents the shear band, and the blue area represents the undisturbed region.

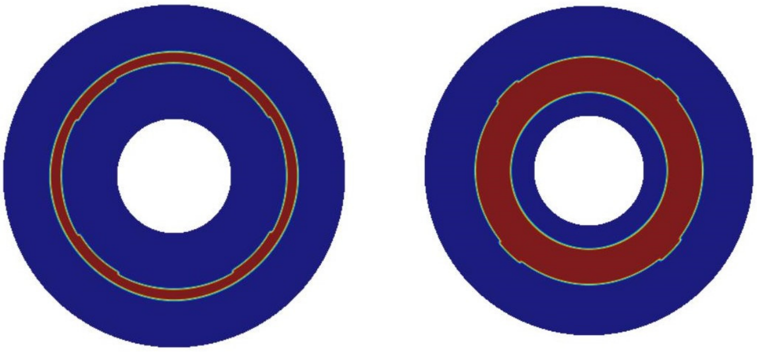

(**a**) H = 1.0 cm (**b**) H = 3.0 cm

(**c**) H = 6.0 cm

Figure 9. Numerical simulation of fine sand: (**a**) stacking height is 1.0 cm; (**b**) stacking height is 3.0 cm; (**c**) stacking height is 6.0 cm.

3.2.2. Characteristics of Shear Bands

In all the numerical results, there is a common feature wherein the starting point of the shear band is located at the boundary between the inner and outer cylinder. However, with the change in parameters, the distribution of the shear band still presents different characteristics:

i. For samples of the same strength when the stacking height is smaller (H = 0.5 cm), the shear band develops vertically upward, and an obvious annular shear band can be seen on the surface (Figure 10a); when the stacking height is larger (H = 1.0 cm), the shear band can only develop upward to a certain height but cannot reach the surface (Figure 10b). When the stacking height is larger (H = 2.0 cm), the shear band can only develop along the bottom and toward the inner cylinder (Figure 10c).

(**a**) H = 0.5 cm

(**b**) H = 1.0 cm

(**c**) H = 2.0 cm

Figure 10. Shear band distribution: (**a**) stacking height is 0.5 cm; (**b**) stacking height is 1.0 cm; (**c**) stacking height is 2.0 cm.

Figure 10a–c shows the distribution of the shear band in the radial section. The section is taken vertically along the direction of the diameter (the hollow part is the rotating shaft).

ii. For samples of the same stacking height, the lower the strength, the more conducive it is to the vertical upward evolution of the shear band (Figure 11a); then, with the increase in strength, the height of the shear band decreases (Figure 11b). For higher strengths, the shear band can only develop along the bottom toward the inner cylinder, similar to characteristic i (Figure 11c).

(**a**) $\varphi = 10°,\ c = 0.25\text{MPa}$

(**b**) $\varphi = 10°,\ c = 0.50\text{MPa}$

(**c**) $\varphi = 10°,\ c = 2.0\text{MPa}$

Figure 11. Shear band distribution: (**a**) strengths for $\varphi = 10$, $c = 0.25$ MPa; (**b**) strengths for $\varphi = 10$, $c = 0.50$ MPa; (**c**) strengths for $\varphi = 10$, $c = 2.0$ MPa.

3.2.3. Stress and Strain Distribution

Why do the shear bands have the above characteristics? We believe that it is determined by the distribution of stress and strain. At the starting point of the shear band, the local strain generated by ring shear is relatively large, which reduces the local modulus due to damage. Under the mechanism of force balance and deformation coordination, the local shear stress will inevitably transfer to the adjacent area, which leads to the expansion of the shear band.

Here, the distribution of shear stress and strain of the section in Figure 11a–c is given. According to the symmetry, only the shear stress and strain on the left of each figure in Figure 11 are given. The shear stress and strain are taken as components perpendicular to the paper surface, and the distribution of different heights from the bottom in each section is shown in Figure 12 (Figure 12a–c corresponds to the shear stress and strain distribution in Figure 11a–c, respectively). The origin of the abscissa starts at the outer edge of the outer shear cylinder.

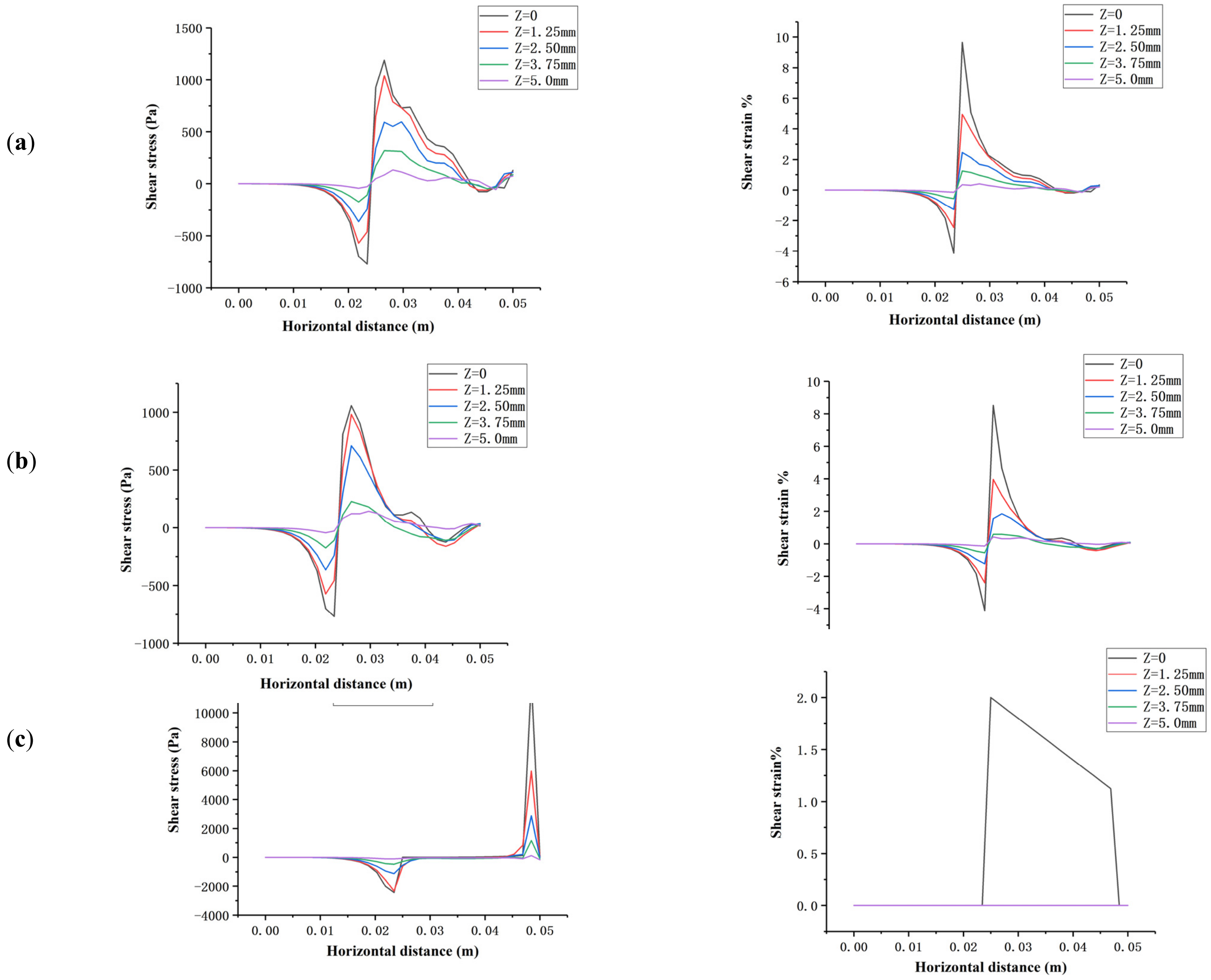

Figure 12. Distribution of shear stress and shear strain on the section: (**a**) shear stress and strain for Figure 11a; (**b**) shear stress and strain for Figure 11b; (**c**) shear stress and strain for Figure 11c.

According to Figure 12, shear stress and strain upheaval occurred at the boundary between the inner and outer cylinders. However, on different sides of the boundary, the shear stress direction is different, thus making a large shear stress difference which is conducive to the generation of a shear band. Furthermore, the shear stress amplitudes are also different. Shear stress in the direction of the inner cylinder is greater than that in the direction of the outer. This confirms that the starting point of the shear band is located at the boundary between the inner and outer cylinders and the evolution of the shear band points to the direction of the inner cylinder. Moreover, it shows that only in the region of the outer cylinder is there shear stress of the same direction, while in the region of the inner cylinder, there is a large shear strain only near the bottom. This indicates that the shear damage occurred only near the bottom of the inner cylinder and did not develop along the height direction when the sample strength was large. In Figure 12c, the strain at the bottom (Z = 0) is much greater than the strain at the other heights, so the other strains appear to be identical and close to zero.

Figure 13 shows the shear stress–strain relationship at the junction of the inner and outer cylinder at the bottom (since it is the point where the shear band starts), for the case of the hydrate ring-shear test (Figure 8b). It can be seen that with the increase in shear strain, when shear damage occurs, the shear stress sharply drops, and then when the strain continues to increase, the shear stress is basically an unloading process.

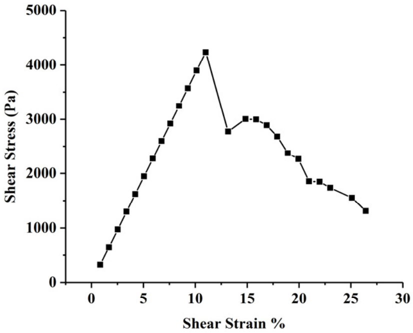

Figure 13. Shear stress–strain relationship.

3.2.4. Variation Law of Geometry Characteristics of Shear Band

Summarizing all the results of experiments and simulations we obtained a dimensionless number $(c + \rho gH \cdot tg\varphi)H/\alpha GL$, which controls the formation and evolution of shear band. In the control number c and φ are the cohesion and friction angle, ρ is density, H is the stacking height, L is the radial width of the shear cylinder (the total radial width of the inner and outer cylinder), G is shear modulus, and α is rotation angle. It can be seen that $(c + \rho gH \cdot tg\varphi)H$ represents the stiffness due to strength, while αGL represents the shear stiffness due to load. This means that the spatial distribution of the shear band is controlled by the ratio of strength stiffness to load stiffness.

Furthermore, it shows that stacking height H is a sensitive variable that reflects the influence of gravity in the form of H^2. The control number $(c + \rho gH \cdot tg\varphi)H/\alpha GL$ determines the geometry characteristics of the shear band, i.e., shear-band width w and height d, here expressed as dimensionless parameters w/L and d/H, respectively.

Now define $K = (c + \rho gH \cdot tg\varphi)H/\alpha GL$, for geomaterials generally G is much higher than the strength value. For expression convenience, the paper takes the value of $\mathrm{K} = (c + \rho gH \cdot tg\varphi)H \times 10^3/\alpha GL$. Therefore, according to the numerical results of multiple schemes, the variation relationship between $w/L \sim$ K and $d/H \sim$ K can be obtained, as shown in Figures 14 and 15.

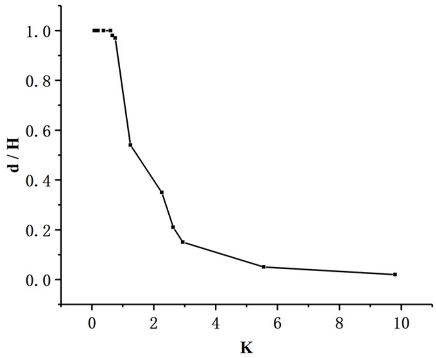

Figure 14. Variation in shear-band width.

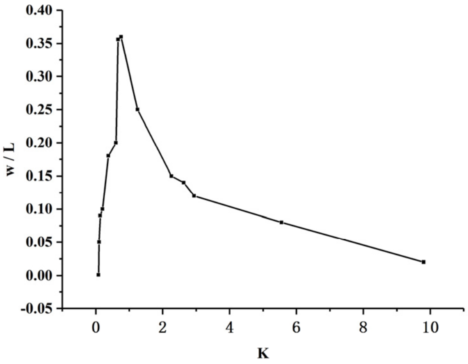

Figure 15. Variation in shear-band height.

According to Figure 14, when K is relatively small the shear band can develop to the surface, as shown in Figure 11a. With the increase in K, the shear band can only develop to a certain height below *H*. When K is much larger, the evolution of the shear band in the vertical direction is very small, until it is close to zero. According to Figure 15, when K is relatively small, the width of the shear band increases with the increase in *K* and then starts to decrease after it reaches the highest value, indicating that there is a critical value which is most conducive to the evolution of the shear band in vertical and horizontal directions. As K continues to grow, the shear band can only be confined to a narrow range near the lateral wall of the inner cylinder.

4. Conclusions and Discussion

Based on the research work in the paper, it is concluded that:

(1). On the basis of ring-shear tests, the basic phenomena of shear bands for dry sand and hydrate were observed, and the shear band evolution mechanism was illustrated;

(2). A dimensionless number *K* is obtained to characterize the evolution process and distribution of the shear band, and it can be used to quantitatively describe the variation law of height and width;

(3). In this paper, the constitutive model used in the numerical simulation needs to be improved. For geomaterials, a continuous model is not entirely appropriate for describing the deformation; perhaps a discrete model is more accurate. Furthermore, the conclusions obtained in this paper are applicable to ring shear under a low deformation rate; if the deformation rate is high, it is likely to produce some different results.

Author Contributions: Conceptualization, X.L. and J.Q.; methodology, X.L.; software, J.Q.; validation, J.Q., X.L. and X.Z.; formal analysis, J.Q.; investigation, J.Q.; resources, X.L. and X.Z.; data curation, X.Z.; writing—original draft preparation, J.Q.; writing—review and editing, X.Z.; visualization, X.L.; supervision, X.Z.; project administration, X.L.; funding acquisition, X.L. and X.Z. All authors have read and agreed to the published version of the manuscript.

Funding: This research was funded by [National Natural Science Foundation of China] grant number [12072347] and [11872365].

Institutional Review Board Statement: Not applicable.

Informed Consent Statement: Not applicable.

Data Availability Statement: Not applicable.

Conflicts of Interest: The authors declare no conflict of interest.

References

1. Latzel, M.; Luding, S.; Herrmann, H.J.; Howell, D.W.; Behringer, R.P. Comparing simulation and experiment of a 2D granular Couette shear device. *Eur. Phys. J. E* **2003**, *11*, 325–333. [CrossRef] [PubMed]
2. Lu, X.; Wang, Y.; Wang, S.; Cui, P. On the shear bandwidth in saturated soils. *Acta Mech. Sin.* **2005**, *37*, 87–91.
3. Borja, R.I.; Song, X.; Rechenmacher, A.L.; Abedi, S.; Wu, W. Shear band in sand with spatially varying density. *J. Mech. Phys. Solids* **2012**, *61*, 219–234. [CrossRef]
4. Lobo-Guerrero, S.; Vallejo, L.E. Modelling Granular Crushing in ring shear tests: Experimental and numerical analyses. *Soils Found.* **2006**, *46*, 147–157. [CrossRef]
5. Wang, B.; Wang, T.; Sun, J.; Shi, J. Shearing characteristic of sliding zone soil from ring shear tests for large scale mudstone landslides in Huangshui River basin. *J. Eng. Geol.* **2017**, *25*, 124–131.
6. Suzuki, M.; van Hai, N.; Yamamoto, T. Ring shear characteristics of discontinuous plane. *Soils Found.* **2017**, *57*, 1–22. [CrossRef]
7. Lv, X.; Zhang, B.; Zhang, P. Laboratory ring shear tests for shear strenghth of sand and clay mixtures. *J. Eng. Geol.* **2019**, *27*, 1110–1115.
8. Zhang, Y.; Guo, C.; Yang, Z.; Shen, Y.; Wu, R.A.; Ren, S. Study on shear strength of deep-seated sliding zone soil of Zhouchangping landslide in Maoxian, Sichuan. *J. Eng. Geol.* **2021**, *29*, 764–776.
9. Cundall, P.A.; Strack, O.D.L. A discrete numerical model for granular assemblies. *Geotechnique* **1979**, *29*, 47–65. [CrossRef]
10. Jiang, M.J.; Peng, D.; Shen, Z.F.; Zhang, W. DEM analysis on formation of shear band of methane hydrate bearing soils. *Chin. J. Geotech. Eng.* **2014**, *36*, 1624–1630.
11. Huang, W. Discrete Element Simulation of Shear Zone Evolution and Characteristics in Sandy Media. Ph.D. Thesis, South China University of Technology, Guangzhou, China, 2015.
12. Jin, W.; Klinger, J.L.; Westover, T.L.; Huang, H. A density dependent Drucker-Prager/Cap model for ring shear simulation of ground loblolly pine. *Powder Technol.* **2020**, *368*, 45–58. [CrossRef]
13. Fenistein, D.; van de Meent, J.W.; van Hecke, M. Universal and wide shear zones in granular bulk flow. *Phys. Rev. Lett.* **2004**, *92*, 094301. [CrossRef] [PubMed]
14. Liang, G.; Zhou, Y.; Gu, Q. *Finite Element Language and Its Application I*; Science Press: Beijing, China, 2016.
15. Erlin, W.; Houzhen, W.; Rongtao, Y. Constitutive model for gas hydrate-bearing sediments considering damage. *Chin. J. Rock Mech. Eng.* **2012**, *31* (Suppl. S1), 3045–3050.
16. Weibull, W. A statistical distribution function of wide applicability. *J. Appl. Mech.* **1951**, *18*, 293–297. [CrossRef]